Journal of Power Sources 444 (2019) 227292

Contents lists available at ScienceDirect

Journal of Power Sources

journal homepage: www.elsevier.com/locate/jpowsour

$La_2Ni_{1-x}Co_xO_{4+\delta}$ ($x = 0.0$, 0.1 and 0.2) based efficient oxygen electrode materials for solid oxide electrolysis cells

V. Vibhu [a,*], I.C. Vinke [a], R.-A. Eichel [a,b], J.-M. Bassat [c], L.G.J. de Haart [a]

[a] Institute of Energy and Climate Research, Fundamental Electrochemistry (IEK-9), Forschungszentrum Jülich GmbH, 52425, Jülich, Germany
[b] Institute of Physical Chemistry, RWTH Aachen University, 52074, Aachen, Germany
[c] CNRS, Université de Bordeaux, Institut de Chimie de La Matière Condensée de Bordeaux (ICMCB), 87 Av. Dr Schweitzer, F-33608, Pessac Cedex, France

HIGHLIGHTS

- $La_2Ni_{1-x}Co_xO_{4+\delta}$ nickelates as O_2-electrode materials for SOEC is reported first time.
- These nickelates are stable and always over-stoichiometric in air/O_2 atmospheres.
- Single cell with $La_2Ni_{0.8}Co_{0.2}O_{4+\delta}$ oxygen electrode shows the best cell performance.
- Lowest degradation is observed for $La_2Ni_{0.8}Co_{0.2}O_{4+\delta}$ electrode under SOEC operation.

GRAPHICAL ABSTRACT

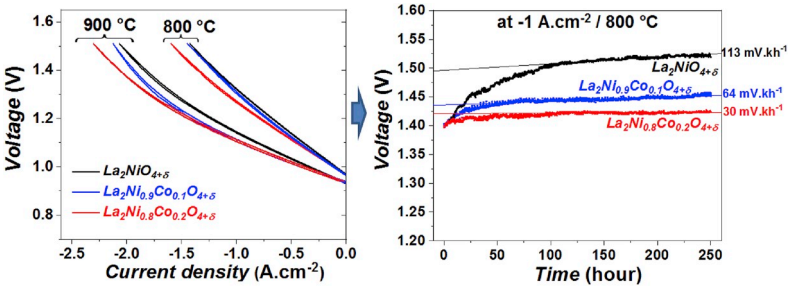

ARTICLE INFO

Keywords:
Nickelates
SOECs
Oxygen over-stoichiometry
Single cell performance
Durability
Degradation

ABSTRACT

The present study is focused on the development of alternative oxygen electrodes for Solid Oxide Electrolysis Cells (SOECs). Rare earth nickelates with general formula $Ln_2NiO_{4+\delta}$ (Ln = La, Pr or Nd) have shown good performance as oxygen electrodes with various electrolytes. Among them, $La_2NiO_{4+\delta}$ is most stable nickelate by itself however its electrochemical performance is lower compare to $Pr_2NiO_{4+\delta}$. Therefore, to further enhance the physico-chemical properties, electrochemical performance of $La_2NiO_{4+\delta}$ as SOECs oxygen electrode, herein, we have performed the substitution of nickel with cobalt. Three compositions ($x = 0.0$, 0.1 and 0.2) were mainly considered and completely characterized using several techniques. The symmetrical as well as single cells were then prepared and electrochemically characterized using DC- and AC-techniques in the temperature range 700–900 °C. The electrode reaction mechanism was also investigated by recording the impedance spectra at different pO_2. With cobalt substitution, an improvement in electrochemical performance as well lower degradation rate is observed during long term SOEC operation at -1 A·cm^{-2} current density at 800 °C with 50% H_2 and 50% H_2O feed gas mixture.

1. Introduction

A variety of energy sources, including renewables, can be used to produce hydrogen, and one way to transform renewable and other non-fossil sources of energy into hydrogen is water electrolysis [1–3]. High temperature electrolysis of steam (HTE) using solid oxide electrolysis cells (SOECs) is expected to consume less electrical energy as compared to electrolysis at low temperature as consequence of the more favourable

* Corresponding author.ss
E-mail address: v.vibhu@fz-juelich.de (V. Vibhu).

https://doi.org/10.1016/j.jpowsour.2019.227292
Received 5 August 2019; Received in revised form 21 September 2019; Accepted 10 October 2019
Available online 17 October 2019

thermodynamic and electrochemical kinetic conditions for the reaction. In solid oxide cells (SOCs) operation, electrode polarizations induce large voltage losses especially at the oxygen electrode [4,5], therefore the modification in the existing materials as well as investigation of new oxygen electrode materials are still under progress.

With respect to oxygen electrode, two kinds of Mixed Ionic and Electronic Conducting (MIEC) oxide materials have been extensively studied; the first one concerns oxygen deficient perovskite materials *e.g.* LSCF ($La_{0.6}Sr_{0.4}Co_{0.2}Fe_{0.8}O_{3-\delta}$) and LSC ($La_{0.6}Sr_{0.4}CoO_{3-\delta}$) [6–14]. However, these materials are less promising due to Sr-segregation especially when the cell is operated during long term [15–17]. Another type of MIEC oxides deals with oxygen over-stoichiometry, *e.g.* nickelates $Ln_2NiO_{4+\delta}$ (Ln = La, Pr, Nd) [18–21]. These compounds with the K_2NiF_4-type layered structure are promising due to their high anionic bulk diffusion as well as surface exchange coefficients, combined with good electrical conductivity and thermal expansion properties matching with those of electrolyte materials *e.g.* yttria-stabilized zirconia (YSZ) or gadolinium doped ceria (GDC) [22–24]. The structure of these nickelates consists of alternate layer of NiO_2 square plane layers and Ln_2O_2 rock salt type layers. This kind of structure has strong capability to accept interstitial oxygen located in rock-salt layer leading to a mixed valance of Ni *i.e.* Ni^{2+} and Ni^{3+} and hence mixed electronic and ionic conductivity (e^-/O^{2-}) [25,26]. In such nickelates, the transport properties are highly dependent on the amount of interstitial oxygen *i.e.* δ-value. For instance, $Pr_2NiO_{4+\delta}$ (PNO) shows a large amount of interstitial oxygen ($\delta \sim 0.25$) compare to $La_2NiO_{4+\delta}$ (LNO) ($\delta \sim 0.16$) [27] and hence PNO shows better conductivity (both ionic and electronic), oxygen diffusivity, surface exchange and electrochemical properties [27]. Despite of good electrochemical properties of $Pr_2NiO_{4+\delta}$ its chemical stability is always an issue [28], while $La_2NiO_{4+\delta}$ is highly chemically stable by itself but has lower electrochemical performance [29].

The present work is focused on cobalt substituted lanthanum nickelates $La_2Ni_{1-x}Co_xO_{4+\delta}$ ($x = 0.0$, 0.1 and 0.2) (LNCO) and aims particularly at the enhancement of electrochemical activity and durability of LNO used as oxygen electrode in SOECs. At first, the preliminary structural and physicochemical characterizations including chemical stability and evolution of the δ-value with temperature and atmosphere (air and oxygen) of LNCO phases are studied. Further the electrochemical behaviour of these materials are investigated with symmetrical half-cells. Finally the electrochemical performance and short term durability test under SOECs conditions are investigated using single cells.

2. Experimental

2.1. Powder preparation

Three compositions of the $La_2Ni_{1-x}Co_xO_{4+\delta}$ ($x = 0.0$, 0.1 and 0.2) were prepared using a solid state synthesis route. The corresponding precursors were La_2O_3 (Aldrich chem, 99.9%), NiO (Alfa Aesar, 99%) and Co_3O_4 (Alfa Aesar, 99%). La_2O_3 powder was pre-fired in a first step at $T = 900\,^{\circ}C$ overnight to remove the water content, due to its high hygroscopic character. The precursors were weighed according to the composition of nickelates and then ball milled for 4 h at 250 rpm using zirconia balls and isopropanol (VWR, 99.8%). After drying at 80 °C overnight, the final annealing was performed at 1300 °C for 12 h in air, leading to well crystallized phases. The nickelates with more than 20% cobalt content were not considered in this work due to instability of the layered structure in air/oxygen atmosphere. The obtained powders were crushed and milled again with zirconia balls and isopropanol for 8 h with the aim to obtain a mean particle size of about 1 μm (as checked using particle size distribution and SEM).

2.2. X-ray diffraction analysis

The powders were first investigated by X-Ray diffraction (XRD) at room temperature using a PANanalytical X'pert MPD diffractometer with Cu-K_α incident radiation to check the purity of phase. Each X-ray diffractogram was fitted by profile matching using the Fullprof software and Rietveld Refinements were carried out.

2.3. Microstructure analysis

The morphologies of the materials were analysed using a Scanning Electron Microscope (Quanta FEG 650, FEI equipped with an EDS detector) operating at 10 kV. The particle size distributions were analysed by laser diffraction particle size analyser (HORBIA, LA-960).

2.4. Thermo gravimetric analysis (TGA)

TGA experiments were carried out using a TA Instrument® TGA-5500 device, with the aim to determine the delta value, δ, at room temperature under air and then its variation as a function of temperature under air and oxygen. In the first case the powders were equilibrated under air up to 1000 °C, then cooled down to room temperature with a slow rate (2 °C·min^{-1}), this cycle being reproduced twice to ensure a stable state of the material, *i.e.* a reproducible oxygen content. Then, a second cycle was performed under Ar - 5% H_2 flux with a very slow heating rate of (0.5 °C·min^{-1}), the decomposition of the material leading to the determination of the oxygen stoichiometry after cycling the sample down to room temperature (La_2O_3, metallic Ni and Co being formed as verified by XRD after the thermal cycle). The variation of the oxygen stoichiometry of the materials was studied either under air or oxygen atmosphere. For this purpose, the powders were first thermodynamically equilibrated under air in the TGA device as described above (*i.e.* two cycles were performed). Then the gas was changed from air to oxygen at high temperature (1000 °C) for faster solid/gas reactivity and kept for 6 h to achieve the equilibrium, and then two cycles were performed under oxygen.

2.5. Dilatometry measurements

Thermal variations of the relative expansion of dense pellets (dL/L) were carried out in the temperature range 35–1000 °C, under air using a differential dilatometer (Netzsch® 402 C), with the aim to determine the TECs of the materials.

2.6. Conductivity measurements

The electrical conductivity of these materials were determined under air using the four-probe technique, in the temperature range 25–850 °C with the heating and cooling rate of 1 °C·min^{-1}. The nickelates were previously sintered at 1350 °C for 6 h in order to get dense pellets.

2.7. Cell preparation

Symmetrical half cells, electrode//GDC//8YSZ//GDC//electrode, were prepared for the electrochemical studies. Terpineol-based slurries were prepared with each nickelate material and with gadolinium doped ceria *i.e.* $Ce_{0.8}Gd_{0.2}O_{2-\delta}$ (GDC) powder (CerPoTech). First, GDC layers (thickness ~ 3–4 μm, ∅ ~ 12 mm) were symmetrically screen printed on both sides of the dense supports of 8 mol% of yttria stabilized zirconia (8YSZ) with diameter ~20 mm and thickness ~300 μm and sintered at 1350 °C for 1 h under air. This dense and thin GDC buffer layer was deposited in order to avoid the reactivity between electrode and 8YSZ [19]. The nickelate layer (thickness ~ 15–20 μm ∅ ~10 mm) was afterwards deposited using the same method and sintered at 1200 °C for 1 h under air. The sintering temperature (1200 °C) was optimized for LNO, to obtain a controlled homogenous porous electrode

microstructure. The same conditions are used for preparing the Co-doped nickelates.

2.8. Electrochemical characterization

The electrochemical measurements were performed under air, using a two electrodes configuration with signal amplitude of 50 mV under zero current condition with the aim to determine the R_p values.

The single cell measurements were performed using NiO-YSZ supported cells (NiO-YSZ//YSZ//GDC//electrode, CeramTec®, ASC-10C type). Anode layers *i.e.* nickelates were deposited by screen printing and sintered at 1200 °C for 1 h under air. For the measurement, Gold and Nickel grids (1.024 cm^{-2} mesh) were used as current collectors for oxygen electrode and fuel electrode respectively. The *i-V* characteristic was measured in electrolysis mode from OCV to 1.5 V with a 50% H_2O and 50% H_2 gas mixture in the temperature range of 700–900 °C. The impedance diagrams were recorded at OCV and from 1.0 to 1.5 V with an increase of 0.1 V, under potentiostatic control with 50 mV *ac* amplitude, from 10^6 Hz down to 10^{-1} Hz, using IVIUM VERTEX potentiostat/galvanostat with integrated frequency response analyser module. The complex impedance diagrams were fitted using an equivalent circuit by means of the RelaxIS® software. The polarization resistance R_p values were calculated from the difference between the low frequency (LF) and the high frequencies (HF) diagram intercepts with the real axis of the Nyquist representation.

3. Results and discussion

3.1. XRD analyses

The XRD study shows that all three nickelates are single phases, their patterns being indexed with an orthorhombic cell described by the *Fmmm* space group. Furthermore, full pattern matching was carried out using the FULLPROF software with the aim to find the lattice parameters. As an example, for $La_2Ni_{0.9}Co_{0.1}O_{4+\delta}$ (LNCO10) and $La_2Ni_{0.8}Co_{0.2}O_{4+\delta}$ (LNCO20), a good agreement is obtained between the experimental and refined patterns (Fig. 1). The obtained cell parameters and unit cell volume are reported in Table 1.

An increase in the lattice parameters *a* and *b* is observed while a decrease is observed in lattice parameter *c*. The decrease in c is large compare to an increase in *a* and *b*, as a result the overall volume of the cell decreases with the cobalt substitution. This behaviour is good agreement with the size of ionic radius of Co and Ni. As the ionic radius of Ni^{2+} (0.69 Å) is higher than Co^{2+} (0.65 Å), the cobalt substitution leads to decreases the overall volume of the cell [30].

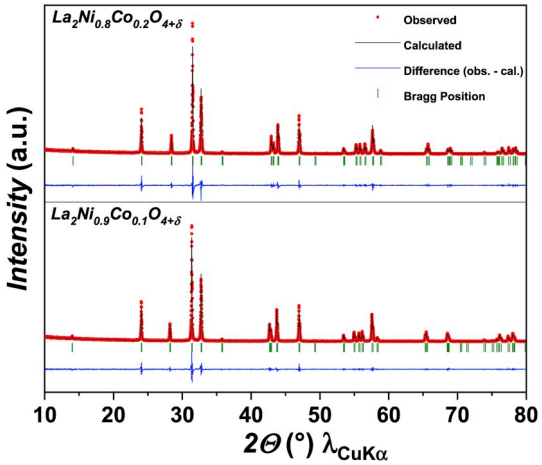

Fig. 1. Fullprof refinement of X-ray patterns of $La_2Ni_{0.9}Co_{0.1}O_{4+\delta}$ ($\chi^2 = 2.33$) and $La_2Ni_{0.8}Co_{0.2}O_{4+\delta}$ ($\chi^2 = 2.89$) using *Fmmm* space group.

Table 1
Lattice parameters a, b, c and space groups of $La_2Ni_{1-x}Co_xNiO_{4+\delta}$

Samples	a (Å)	b (Å)	c (Å)	V (Å^3)	Space Group
$La_2NiO_{4+\delta}$	5.459 (3)	5.463 (4)	12.685 (4)	378.41 (3)	*Fmmm*
$La_2Ni_{0.9}Co_{0.1}O_{4+\delta}$	5.464 (4)	5.468 (3)	12.648 (5)	378.21 (4)	*Fmmm*
$La_2Ni_{0.8}Co_{0.2}O_{4+\delta}$	5.472 (3)	5.476 (3)	12.610 (2)	377.98 (3)	*Fmmm*

3.2. Thermo Gravimetric analysis

3.2.1. Determination of δ of material equilibrated under air

The oxygen over-stoichiometry (δ) at room temperature for LNCO phases was calculated using the results of TGA experiments performed under reducing conditions (Ar−5% H_2 atmosphere, heating rate 0.5 °C·min^{-1}). The thermal variation of weight loss as a function of temperature is reported in Fig. 2a. As earlier reported [31], two weight losses occur. The first one, around 400 °C, corresponds to the reduction of Ni^{3+}/Co^{3+} into Ni^{2+}/Co^{2+} (the oxygen over-stoichiometry being reduced down to $\delta = 0$ when expecting only La^{3+} cations). The second weight loss characterizes the complete reduction of LNCO in appropriate ratio (*i.e. x* dependent) into La_2O_3, Ni and Co, leading to the determination of 4+δ. The value of δ was as well calculated *via* iodometric titration [25]. The δ values calculated by iodometry and TGA are gathered in Table 2. An increase of δ is observed with Co substitution, from 0.16 (LNO) to 0.20 (LNCO20). The values of δ in this study are in good agreements with the earlier reported results [31].

The thermal variations of the oxygen content, 4+δ, for the $La_2Ni_{1-x}Co_xO_{4+\delta}$ phases under air and oxygen atmospheres are plotted in Fig. 2b and c, respectively. In both atmospheres, all LNCO nickelates show reversible oxygen exchange and remain always oxygen over-stoichiometric ($\delta > 0$) over the whole temperature range confirming MIEC properties under air and oxygen atmosphere. For instance, in air the δ-values are 0.06, 0.08 and 0.10 for LNO, LNCO10 and LNCO20 respectively at 1000 °C. A sudden decrease of oxygen content around $T \approx 270$ °C is evident under air for all LNCO phases (Fig. 2b). This discontinuity may be ascribed to the structural phase transition from the orthorhombic to the tetragonal phase [24]. In addition for LNO, δ decreases from 0.11 to 0.08 at operating temperature of solid oxide cells (600 − 800 °C) which is in good agreement with Nakamura *et al.* [32]. In oxygen atmosphere, an uptake of oxygen content is observed for all nickelates which lead to increase in the δ-values (Fig. 2c). For instance, δ increases from 0.16 to 0.25 for LNO at room temperature. However, all these materials are stable in oxygen atmosphere, as confirmed by the XRD after the TGA experiment.

3.2.2. Dilatometry measurements

The thermal variations of the relative expansion *dL/L* measured under air for LNCO phases are reported in Fig. 3. The thermal expansion coefficients (TECs), calculated from the slope of the corresponding straight lines in the full range of temperature indicates a slight increase in TEC with cobalt substitution. The TEC value obtained for LNO is 13.1×10^{-6} °C^{-1}, which increases up to 15×10^{-6} °C^{-1} for LNCO20. Therefore from a thermo-mechanical point of view these nickelates can be used as oxygen electrode in solid oxide cells involving 8YSZ as well as GDC as electrolytes [24]. The chemical expansion contribution has not been considered as a significant feature due to the absence of a major deviation of the dL/L *vs.* T. This is in agreement with previously reported works, indicating almost zero chemical expansion coefficients for K_2NiF_4 -type phases [32,33].

3.2.3. Electrical conductivity measurements

The variations of the total electrical conductivity *σ vs.* 1000/*T* under air for LNCO compounds are reported in Fig. 4.

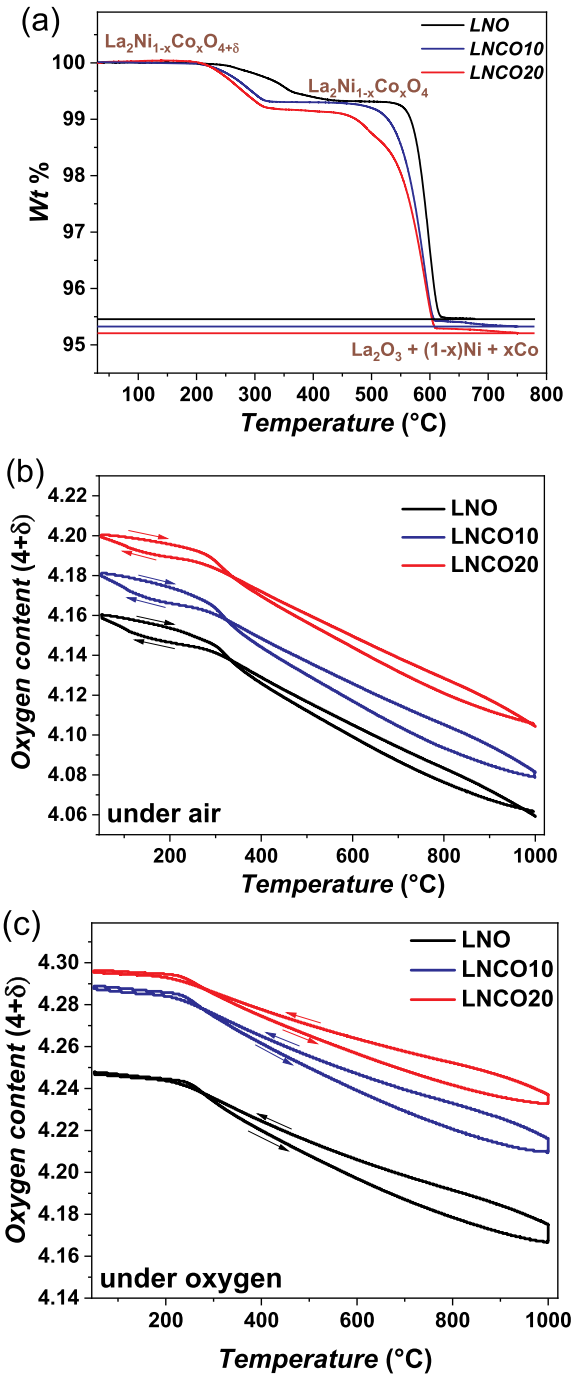

Fig. 2. (a) Weight loss curve in Ar–5%H_2 atmosphere, thermal variation of the oxygen content (4+δ) (b) in air and (c) in oxygen atmosphere (50 °C ≤ T ≤ 1000 °C), for $La_2Ni_{1-x}Co_xO_{4+\delta}$ phases.

Table 2
Oxygen over-stoichiometry δ calculated from TGA and iodometry measurements, and the average δ value.

Nickelates	δ (by TGA)	δ (by Iodometry)	δ (average)
$La_2NiO_{4+\delta}$	0.16	0.16	0.16
$La_2Ni_{0.9}Co_{0.1}O_{4+\delta}$	0.176	0.18	0.18
$La_2Ni_{0.8}Co_{0.2}O_{4+\delta}$	0.20	0.195	0.20

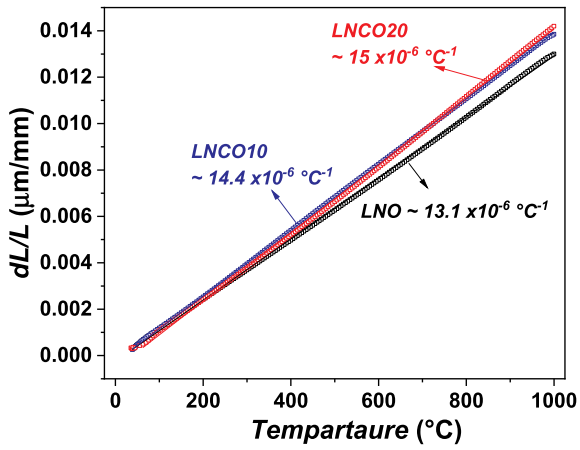

Fig. 3. Thermal variation of the relative expansion (dL/L) with temperature (30 °C ≤ T ≤ 1000 °C) for $La_2Ni_{1-x}Co_xO_{4+\delta}$ phases under air atmosphere.

All LNCO phases exhibit a semi-conducting behaviour for T < 600 °C, with a maximum of conductivity observed in the 600–800 °C range. At room temperature, LNO shows maximum electrical conductivity (40 S·cm^{-1}), which is in agreement with the previously reported result [18]. With cobalt substitution or increasing cobalt content a decrease in conductivity is observed especially for T < 600 °C. Boehm *et al.* have reported similar results for copper substituted LNO *i.e.* the conductivity decreases with increasing Cu content [18]. Above T > 600 °C, all three phases shows almost similar conductivity value of ~70 S·cm^{-1}. Thus partial substitution of cobalt at the nickel site does not improve the electronic conductivity which is contrary to LSCF based perovskites materials [34].

3.3. Electrochemical measurements

3.3.1. Symmetrical half-cells measurements

The symmetrical cell was mounted into the measurement setup, with flow of air. The cell was heated at 900 °C and the impedance diagrams were investigated by EIS at $i_{dc} = 0$ condition in the temperature range 700–900 °C under air. The R_p values were obtained by fitting the impedance diagrams recorded for all the LNCO half-cells with three R||CPE (constant phase element) in series along with a series resistance R_s, which is the simplest equivalent circuit model that yields a good fit to the data. The variations of calculated total R_p for LNO, LNCO10 and LNCO20 electrodes, as a function of T (Arrhenius plot) are shown in the supplementary information Fig. S1.

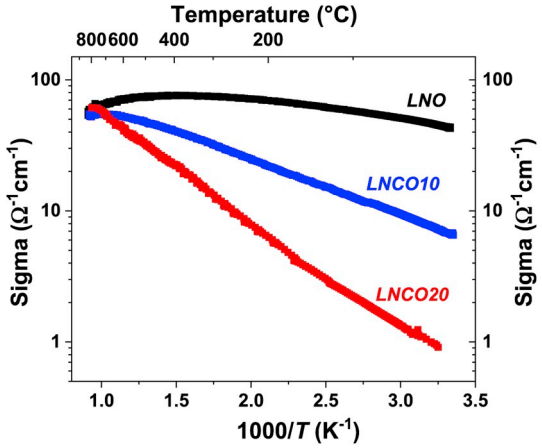

Fig. 4. Thermal variation of the electrical conductivity measured (50 °C ≤ T ≤ 800 °C) under air for $La_2Ni_{1-x}Co_xO_{4+\delta}$ phases.

The electrochemical performance is notably improved (*i.e.* decrease of R_p) by the substitution of Ni by Co, irrespective of the temperature. For instance, a R_p value of 135 mΩ·cm^2 is achieved at 800 °C for LNO while after substitution of Ni by Co, the R_p values decrease down to 88 and 80 mΩ·cm^2 for LNCO10 and LNCO20, respectively (Fig. S1). From those preliminary results, it can be concluded that the best electrochemical property (*i.e.* lowest R_p) is achieved with the LNCO20 electrode. In addition, the obtained R_p value for LNO is in good agreement with the earlier reported results [27]. No data is available in the literature for electrochemical performance of cobalt doped nickelates.

Furthermore, the activation energies (*E*a) are calculated from the slopes of R_p *vs.* reciprocal temperature curves. A slight increase in activation energy is observed with cobalt substitution, for instance, the activation energies are 1.13, 1.21 and 1.26 eV respectively for LNO, LNCO10 and LNCO20 half-cells. In general, an increase in activation energy is observed with increasing cobalt content. Lim *et al.* have shown that the activation energy values for $Ba_{0.5}Sr_{0.5}Co_xFe_{1-x}O_3$ (BSCF) were 0.95, 1.37, 1.48, and 1.48 eV for $x = 0.2, 0.4, 0.6$ and 0.8 respectively [35]. Nevertheless the activation energy values for LNCO electrodes are far below those from $La_{0.6}Sr_{0.4}Co_{0.2}Fe_{0.8}O_3$ half-cells (1.63 eV) [36].

3.3.2. Determination of rate limiting step in electrode reaction

In order to investigate the effect of cobalt substitution on the electrode reaction mechanism, the impedance measurements were performed under different oxygen partial pressures. At steady state OCV conditions, the polarization resistance of each electrode process depends on the partial pressure of oxygen according to the following relation:

$$R_p = R_p^0 \times (pO_2)^{-m}$$

where the exponent m characterizes the nature of the step involved in the electrochemical reaction [37–40]. The reaction steps with the variation of corresponding exponent m can be described as follows:

a) $m = 0$ characterizes the ionic transfer of O^{2-} ions across the electrolyte-electrode interface and diffusion of O^{2-} oxide ions:

$$O^{2-}{}_{(electrolyte)} \Leftrightarrow O^{2-}{}_{(electrode)}$$

b) $m = ¼$ corresponds to the oxygen surface exchange reaction (charge transfer process), which occurs at the two-phase gas/electrode interface; it involves the oxidation of O^{2-} ions and the adsorption of oxygen at the surface of electrode

$$O_O^x \Leftrightarrow O^{2-}{}_{ads} + V_O^{\bullet\bullet}$$

$$O^{2-}{}_{ads} \Leftrightarrow O_{ads} + 2e^-$$

c) $m = ½$ is related to the association of the desorbed atomic species (O_{ads}) into molecular oxygen ($O_{2,ads}$) at the electro-active sites of the mixed ionic electronic conductor (MIEC) oxide:

$$2\,O_{ads} \Leftrightarrow O_{2\,ads}$$

d) $m = 1$ characterizes the desorption of $O_{2,ads}$ at the active reaction sites according to the given relation and then the diffusion of $O_2(g)$ in the pores of the electrode or above the electrode.

$$O_{2\,ads} \Leftrightarrow O_2\,(g)$$

The variations of impedance spectra with pO_2 at 800 °C for LNO and LNCO20 symmetrical half-cell are shown in Fig. 5a and b. An increase in total polarization resistance is observed with decreasing pO_2. The impedance diagrams were well fitted using three *R||CPE* elements along

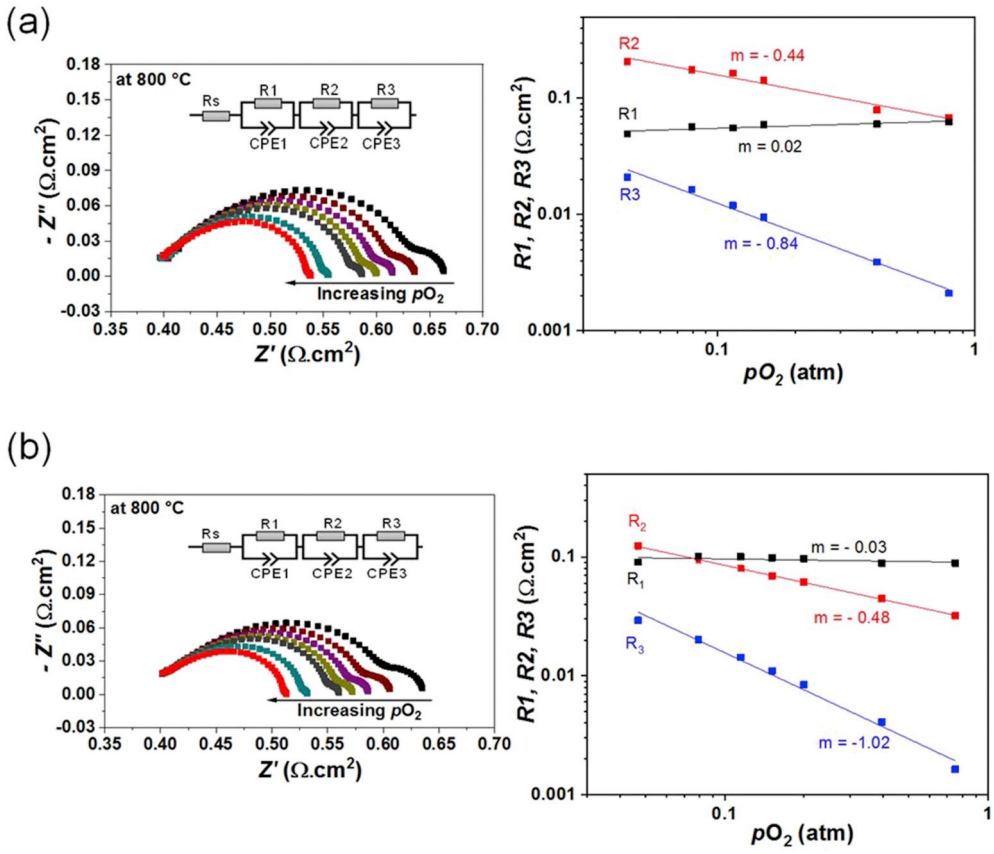

Fig. 5. Variation of impedance spectra and polarization resistances as a function of oxygen partial pressure at 800 °C for (a) LNO and (b) LNCO20 symmetrical half-cells.

with a series resistance R_s.

The variations of R_p of each contribution (R_1, R_2 and R_3) as a function of pO_2 are depicted in Fig. 5a and b. Three different exponents (m) are obtained after performing linear fitting to the three different polarization resistance R_1, R_2 and R_3 for both LNO and LNCO20 symmetrical half-cells.

The exponents m ~0, 0.5 and 1 indicate that the ionic transfer of O^{2-} ions, association of desorbed atomic species into molecular oxygen and the gas diffusion process, respectively are involved for the electrode reaction process for both LNO and LNCO20 symmetrical half-cells. It further indicates that the substitution with cobalt at Ni site does not change the electrode process. The polarization resistance $R_2 > R_1$ at lower pO_2 while at higher pO_2, $R_2 < R_1$ indicates that the electrode reaction may be limited by both O^{2-} ions transfer and the association of desorbed atomic species into molecular oxygen.

3.3.3. Single cell measurements

The single cell was mounted into the measurement setup, with flows of air and N_2 on the anode and cathode sides, respectively. The cell was heated at 900 °C and N_2 at the anode side was progressively replaced by dry hydrogen (H_2) to reduce NiO into metallic Ni. After reduction of the single cell, the OCV under dry condition (9 NL·h^{-1} H_2 and 9 NL·h^{-1} air, on fuel electrode side and oxygen electrode side respectively) was ≈1.21 V at 900 °C for all three cells. Under 50% H_2 and 50% H_2O mixture (4.5 NL·h^{-1} H_2 + 4.5 NL·h^{-1} H_2O and 9 NL·h^{-1} air, on fuel electrode side and oxygen electrode side respectively), the measured OCVs, at 800, 850 and 900 °C are 0.97, 0.955 and 0.94 V, respectively, for LNO single cells. Similar OCVs were also observed for LNCO10 and LNCO20 cells. The decrease in OCV with increase the operating temperature demonstrates that the electrical energy barrier that must be overcome to perform electrolysis decreases with increasing temperature.

The current-voltage characteristics of LNCO single cells at 800 and 900 °C are plotted in Fig. 6. An increase in electrochemical performance is observed with increasing temperature. The cell current densities obtained under the applied voltage of 1.5 V at 900 °C are 2.05, 2.10 and 2.30 A·cm^{-2} respectively for LNO, LNCO10 and LNCO20 single cells, and at 800 °C, the current densities are 1.42, 1.45 and 1.60 A·cm^{-2} respectively for LNO, LNCO10 and LNCO20 single cells (Fig. 6). It is seen that the single cell performance is increasing with increasing cobalt content. It is worth mentioning that the symmetrical half-cell measurements containing LNCO electrodes show similar trend *i.e.* a decrease in total R_p with increasing cobalt content. Among the three cells of LNCO, the best electrochemical performance is observed for the single cell with LNCO20 electrode. The increase in performance with cobalt doping can be understand in terms of transport properties *i.e.* diffusion (D^*) and surface exchange coefficient (k^*). Kilner *et al.* and Munnings *et al.* have reported that the substitution of nickel by cobalt in LNO slightly improves the diffusion coefficient but largely enhances the surface exchange coefficient of the material with remarkable decrease in activation energy [23,31]. As these transport properties are directly linked with the electrochemical properties of the materials, the electrochemical performances of the cells with cobalt doped LNO electrodes are increased.

In addition, the electrochemical performances of LNCO cells were compared with commercial LSCF single cell and it was found that the performance of LNO and LNCO10 cell are comparable with LSCF cell at 800 °C with 1.5 V applied electrolysis voltage. For LNCO20 cell, the performance is higher than that of LSCF cell under same measurement conditions. However, the performance of LSCF is slightly higher than all LNCO cell at 900 °C and at 1.5 V. The behaviour of LNO and LSCF, in this work, is consistent with the earlier reported result. Kim *et al.* have recently compared that the performance of LNO and LSCF and investigated similar behaviour in SOEC mode at 650 °C with 80% H_2O + 20% H_2 gas mixture [41].

Furthermore, the activation energies (E_a) at OCVs conditions are calculated from the slopes of the total electrode resistance (ASR) *vs.* reciprocal temperature curves. Similar trend *i.e.* increase in E_a was also observed for the symmetrical half-cells in 700–900 °C temperature range under OCV conditions (*cf.* Fig. S1). The activation energy is increasing slightly with increasing cobalt content in lanthanum nickelate, as shown in supplementary information Fig. S2. For instance, the activation energies are 0.85, 1.08 and 1.1 eV for LNO, LNCO10 and LNCO20 single cells respectively.

The impedance spectra were also recorded in the 700–900 °C temperature range for all three cells as a function of applied potential and then the total cell resistance (ASR) were calculated. The supplementary information Fig. S3 compares the ASRs of LNO and LNCO20 at 800 and 900 °C (LNCO10 is not plotted for clarity). The ASR of LNCO20 is always lower than that of LNO throughout the temperature range and applied potential. The ASR is dependent on both operating temperature and applied potential. At lower applied potential the ASR is largely dependent on the operating temperature whereas at high applied potential the ASR is less dependent on operating temperature. For instance, the ASR at 1.0 V is 0.18 and 0.28 Ω·cm^2 at 900 and 800 °C respectively for LNCO20 whereas at 1.5 V, it is 0.49 and 0.54 Ω·cm^2 at 900 and 800 °C respectively. The change in ASR value is consistent with the slope of voltage-current density curve. It is also observed that the ohmic resistance, exhibited as the first intercept with real axis, doesn't show much change with applied potential. Consequently, the increased performance of LNCO20 cell is mainly attributed to the enhanced electrode reaction.

3.3.4. Durability test with single cells

The durability operations of LNCO cells for steam electrolysis were galvanostatically carried out in the electrolysis mode. Fig. 7 depicts the stability of the single cell measured at 800 °C with a high current density

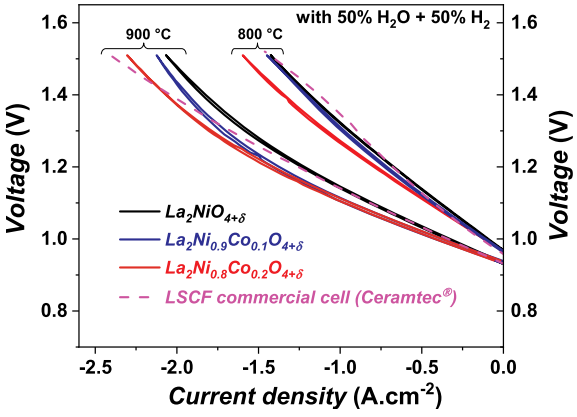

Fig. 6. Voltage *vs.* current density curves for the single cells containing LNO, LNCO10, LNCO20 and LSCF electrodes at 800 and 900 °C.

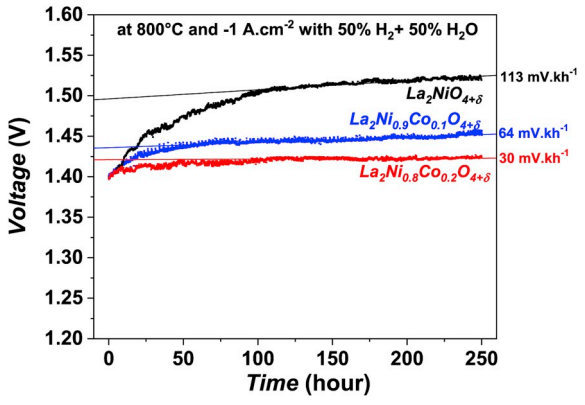

Fig. 7. Durability of LNO, LNCO10 and LNCO20 single cells at 800 °C under current density of −1 A·cm^{-2} with 50% H_2 + 50% H_2O feed gas mixture.

of -1 A·cm^{-2} for 250 h, during which the feed gas mixture of 50% H_2, 50% H_2O with a total flow of 9 NL·h^{-1} was introduced to the fuel electrode.

During the stability test, all three cells experienced degradation, with increase in electrolysis voltage. No significant cell deterioration was observed within the 250 h operation period for all three cells. However the three cells behave differently during the stability test. All cells show a rapid increase initially and then show stable behaviour. The electrolysis voltage increased from 1.41 to 1.52 V for LNO after 250 h, shows highest degradation among all. The degradation rate was estimated (in mV·kh^{-1}) by performing linear fit in the stability region of Voltage *vs.* Time curve and found ~113 mV·kh^{-1} for LNO cell. However, the other two cells show lower degradation rates *i.e.* ~64 mV·kh^{-1} and ~30 mV·kh^{-1}, for LNCO10 and LNCO20 single cell respectively. Remarkably, the LNCO20 single cell shows lowest degradation after 250 h under electrolysis conditions.

Finally it can be concluded that, the substitution with cobalt in LNO enhance the electrochemical activity of the material. The single cell containing LNCO20 electrode shows highest performance with enhanced durability at least up to 250 h at -1 A·cm^{-2} under steam electrolysis conditions.

3.3.5. Post-test analysis of single cell

The single cells were inspected using SEM after electrochemical measurement. Mainly four regions were considered for characterizing the cross section *i.e.* electrolyte, electrodes, electrode/GDC interface and GDC/electrolyte interface (as fuel electrode was same for all three cells). Since, almost no change is observed in the bulk of the electrodes and the electrolyte, the interface electrode/GDC is mainly discussed here. Fig. 8 compares the electrode//GDC//electrolyte interfaces after 250 h operation at -1 A·cm^{-2} under steam electrolysis condition at 800 °C, for LNO and LNCO20 single cells. The backscattered electron images of electrode//GDC//8YSZ//Ni-YSZ single cells are reported in Fig. 8a and b. No delamination or cracks were observed for the all the cells. However, the electrode/GDC interface for LNO and LNCO20 cells seems different. The formation of an interphase between electrode and GDC is clearly observed for both the cells, though, the interphase is quite large for LNO single cell (Fig. 8a), indicating that the inter-diffusion of cations are taking place at the electrode/GDC interface. The formation of new interphase might be ion blocking and could explain the large degradation for LNO single cell. The formation of interphase is also detected for LNCO20 single cell, but lower in extent (Fig. 8b).

Later on to confirm the interphase formation, the reactivity test between LNO and GDC was separately performed at sintering as well as operating temperatures. The powder of LNO and GDC were mixed in the ratio of 50:50 and sintered at 1200 °C/1 h (sintering temperature) and 800 °C/250 h (operating temperature). Various phases were observed by XRD at the sintering temperature including LNO, $La_2Ce_2O_7$, (La,Gd)CeO_2, $La_3Ni_2O_7$ and $La_4Ni_3O_{10}$, as shown in supplementary information Fig. S4. While at the operating temperature *i.e.* (800 °C/250 h), almost no reactivity was observed (Fig. S5). These results indicate that the inter-diffusion of cation mainly occurs at the sintering temperature which further deteriorates the cell performance during long term operation.

4. Conclusion

The present study is focused on alternative oxygen electrodes for SOECs based on K_2NiF_4 structural type $La_2Ni_{1-x}Co_xO_{4+\delta}$ nickelates (LNCO). The selected compositions ($x = 0.0$, 0.1 and 0.2) were successfully synthesized and exist with orthorhombic structure. The δ value increases with increasing x *i.e.* with increasing cobalt content. A decrease in polarization resistance is observed for symmetrical half-cells with increasing cobalt content throughout the temperature range of 700–900 °C under OCV conditions. An increase in electrochemical performance is observed in case of single cells with cobalt substitution. The highest current densities *i.e.* 2.30 and 1.60 A·cm^{-2} at 900 and 800 °C respectively, are observed for $La_2Ni_{0.8}Co_{0.2}O_{4+\delta}$ single cell. During the stability test up to 250 h at 800 °C and -1 A·cm^{-2}, a large degradation is observed for $La_2NiO_{4+\delta}$ single cell. However with cobalt substitution, a stable behaviour is observed. More especially with $La_2Ni_{0.8}Co_{0.2}O_{4+\delta}$ single cell, a very stable behaviour is observed with slight increase in electrolysis voltage (~30mV·kh). Therefore, among all LNCO single cells, the best performance is obtained for $La_2Ni_{0.8}Co_{0.2}O_{4+\delta}$ single cell under electrolysis condition.

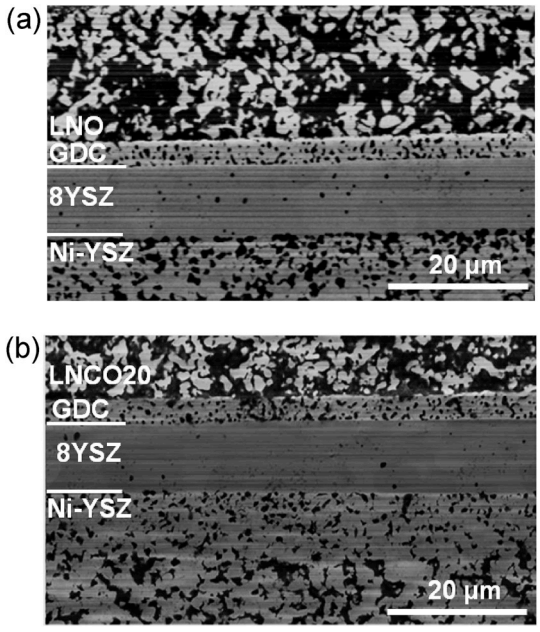

Fig. 8. SEM images after 250 h operation for (a) LNO and (b) LNCO20 single cells at 800 °C under current density of -1 A·cm^{-2} with 50% H_2 + 50% H_2O gas mixture.

Acknowledgments

The results reported here were obtained within the frame of the European project SElySOs. This project has received funding from the Fuel Cells and Hydrogen 2 Joint Undertaking under grant agreement No 671481. This Joint Undertaking receives support from the European Union's Horizon 2020 research and innovation programme and Greece, Germany, Czech Republic, France, Norway.

Appendix A. Supplementary data

Supplementary data to this article can be found online at https://doi.org/10.1016/j.jpowsour.2019.227292.

References

[1] A. Hauch, S.D. Ebbesen, S.H. Jensen, M. Mogensen, J. Mater. Chem. 18 (20) (2008) 2331.
[2] S.H. Jensen, P.H. Larsen, M. Mogensen, Int. J. Hydrogen Energy 32 (15) (2007) 3253.
[3] J. Udagawa, P. Aguiar, N.P. Brandon, J. Power Sources 166 (1) (2007) 127.
[4] J. Park, D. Kim, J. Baek, Y.-J. Yoon, P.-C. Su, S. Lee, Energies 11 (5) (2018) 1204.
[5] O. Yamamoto, Electrochim. Acta 45 (15) (2000) 2423.
[6] L.W. Tai, M.M. Nasrallah, H.U. Anderson, D.M. Sparlin, S.R. Sehlin, Solid State Ion. 76 (3) (1995) 259.
[7] S.J. Kim, G.M. Choi, Solid State Ion. 262 (2014) 303.
[8] G.C. Kostogloudis, C. Ftikos, Solid State Ion. 126 (1) (1999) 143.
[9] M.A. Laguna-Bercero, J.A. Kilner, S.J. Skinner, Chem. Mater. 22 (3) (2010) 1134.
[10] Z. Zhao, L. Liu, X. Zhang, W. Wu, B. Tu, D. Cui, D. Ou, M. Cheng, Int. J. Hydrogen Energy 38 (35) (2013) 15361.
[11] F. Tietz, D. Sebold, A. Brisse, J. Schefold, J. Power Sources 223 (2013) 129.
[12] V. Vibhu, S. Yildiz, I.C. Vinke, R.-A. Eichel, J.-M. Bassat, L.G.J. de Haart, J. Electrochem. Soc. 166 (2) (2019) F102.
[13] S. Diethelm, J.V. Herle, D. Montinaro, O. Bucheli, Fuel Cells 13 (4) (2013) 631.

[14] P. Hjalmarsson, M. Søgaard, M. Mogensen, Solid State Ion. 179 (2008) 27–32, 1422.
[15] K. Chen, S.P. Jiang, J. Electrochem. Soc. 163 (11) (2016) F3070.
[16] D. Oh, D. Gostovic, E.D. Wachsman, J. Mater. Res. 27 (15) (2012) 1992.
[17] L. Zhao, J. Drennan, C. Kong, S. Amarasinghe, S.P. Jiang, J. Mater. Chem. 2 (29) (2014) 11114.
[18] E. Boehm, J.M. Bassat, M.C. Steil, P. Dordor, F. Mauvy, J.C. Grenier, Solid State Sci. 5 (7) (2003) 973.
[19] C. Ferchaud, J.-C. Grenier, Y. Zhang-Steenwinkel, M.M.A. van Tuel, F.P.F. van Berkel, J.-M. Bassat, J. Power Sources 196 (4) (2011) 1872.
[20] X. Tong, F. Zhou, S. Yang, S. Zhong, M. Wei, Y. Liu, Ceram. Int. 43 (2017), 10927.
[21] V. Vibhu, A. Rougier, C. Nicollet, A. Flura, S. Fourcade, N. Penin, J.-C. Grenier, J.-M. Bassat, J. Power Sources 317 (2016) 184.
[22] A. Aguadero, J.A. Alonso, M.J. Martinez-Lope, M.T. Fernandez-Diaz, M. J. Escudero, L. Daza, J. Mater. Chem. 16 (33) (2006) 3402.
[23] C.N. Munnings, S.J. Skinner, G. Amow, P.S. Whitfield, I.J. Davidson, Solid State Ion. 176 (23) (2005) 1895.
[24] A. Flura, S. Dru, C. Nicollet, V. Vibhu, S. Fourcade, E. Lebraud, A. Rougier, J.-M. Bassat, J.-C. Grenier, J. Solid State Chem. 228 (2015) 189.
[25] E. Boehm, J.M. Bassat, P. Dordor, F. Mauvy, J.C. Grenier, P. Stevens, Solid State Ion. 176 (37) (2005) 2717.
[26] V. Vibhu, M.R. Suchomel, N. Penin, F. Weill, J.-C. Grenier, J.-M. Bassat, A. Rougier, Dalton Trans. 48 (1) (2019) 266.
[27] V. Vibhu, A. Rougier, C. Nicollet, A. Flura, J.-C. Grenier, J.-M. Bassat, Solid State Ion. 278 (2015) 32.
[28] A.V. Kovalevsky, V.V. Kharton, A.A. Yaremchenko, Y.V. Pivak, E.N. Naumovich, J. R. Frade, J. Eur. Ceram. Soc. 27 (13) (2007) 4269.
[29] V. Vibhu, J.-M. Bassat, A. Flura, C. Nicollet, J.-C. Grenier, A. Rougier, ECS Trans. 68 (1) (2015) 825.
[30] R.D. Shannon, Acta Crystallogr. A 32 (5) (1976) 751.
[31] J.A. Kilner, C.K.M. Shaw, Solid State Ion. 154–155 (2002) 523.
[32] T. Nakamura, Y. Takeyama, S. Watanabe, K. Yashiro, K. Sato, T. Hashida, J. Mizusaki, ECS Trans. 25 (2) (2009) 2573.
[33] S.R. Bishop, Acta Mech. Sin. 29 (3) (2013) 312.
[34] E.V. Tsipis, V.V. Kharton, J. Solid State Electrochem. 12 (11) (2008) 1367.
[35] Y.H. Lim, J. Lee, J.S. Yoon, C.E. Kim, H.J. Hwang, J. Power Sources 171 (1) (2007) 79.
[36] E. Perry Murray, M.J. Sever, S.A. Barnett, Solid State Ion. 148 (1) (2002) 27.
[37] N. Grunbaum, L. Dessemond, J. Fouletier, F. Prado, L. Mogni, A. Caneiro, Solid State Ion. 180 (28) (2009) 1448.
[38] R. Amin, K. Karan, J. Electrochem. Soc. 157 (2) (2010) B285.
[39] F. Mauvy, J.M. Bassat, E. Boehm, J.P. Manaud, P. Dordor, J.C. Grenier, Solid State Ion. 158 (1) (2003) 17.
[40] G.N. Mazo, N.V. Lyskov, L.S. Leonova, Solid State Ion. 182 (1) (2011) 64.
[41] S.J. Kim, K.J. Kim, A.M. Dayaghi, G.M. Choi, Int. J. Hydrogen Energy 41 (33) (2016) 14498.